The Astrophysical Journal, 897:17 (13pp), 2020 July 1 https://doi.org/10.3847/1538-4357/ab95ff
© 2020. The American Astronomical Society. All rights reserved.

Cosmological Information from the Small-scale Redshift-space Distortion

Motonari Tonegawa[1], Changbom Park[1], Yi Zheng[2], Hyunbae Park (박현배)[1,3,4], Sungwook E. Hong (홍성욱)[5], Ho Seong Hwang[3], and Juhan Kim (김주한)[6]

[1] School of Physics, Korea Institute for Advanced Study, 85 Hoegiro, Dongdaemun-gu, Seoul, 02455, Republic of Korea
[2] School of Physics and Astronomy, Sun Yat-sen University, 2 Daxue Road, Tangjia, Zhuhai, 519082, People's Republic of China
[3] Korea Astronomy and Space Science Institute, 776 Daedeok-daero, Yuseong-gu, Daejeon, 34055, Republic of Korea
[4] Kavli IPMU (WPI), UTIAS, The University of Tokyo, Kashiwa, Chiba 277-8583, Japan
[5] Natural Science Research Institute, University of Seoul, 163 Seoulsiripdaero, Dongdaemun-gu, Seoul, 02504, Republic of Korea
[6] Center for Advanced Computation, Korea Institute for Advanced Study, 85 Hoegiro, Dongdaemun-gu, Seoul, 02455, Republic of Korea; kjhan@kias.re.kr
Received 2019 December 27; revised 2020 May 11; accepted 2020 May 20; published 2020 June 29

Abstract

The redshift-space distortion (RSD) in the observed distribution of galaxies is known as a powerful probe of cosmology. Observations of large-scale RSD, caused by the coherent gravitational infall of galaxies, have given tight constraints on the linear growth rate of the large-scale structures in the universe. On the other hand, the small-scale RSD, caused by galaxy–random motions inside clusters, has not been much used in cosmology, but it also has cosmological information because universes with different cosmological parameters have different halo mass functions and virialized velocities. We focus on the projected correlation function $w(r_p)$ and the multipole moments ξ_l on small scales (1.4–30 h^{-1} Mpc). Using simulated galaxy samples generated from a physically motivated most bound particle (MBP)–galaxy correspondence scheme in the Multiverse Simulation, we examine the dependence of the small-scale RSD on the cosmological matter density parameter Ω_m; the satellite velocity bias with respect to MBPs, b_v^s; and the merger timescale parameter α. We find that $\alpha = 1.5$ gives an excellent fit to the $w(r_p)$ and ξ_l measured from the Sloan Digital Sky Survey–Korea Institute for Advanced Study value-added galaxy catalog. We also define the "strength" of the Fingers of God as the ratio of the parallel and perpendicular size of the contour in the two-point correlation function set by a specific threshold value and show that the strength parameter helps constrain (Ω_m, b_v^s, α) by breaking the degeneracy among them. The resulting parameter values from all measurements are (Ω_m, b_v^s) = (0.272 ± 0.013, 0.982 ± 0.040), indicating a slight reduction of satellite galaxy velocity relative to the MBP. However, considering that the average MBP speed inside halos is 0.94 times the dark matter velocity dispersion, the main drivers behind the galaxy velocity bias are gravitational interactions, rather than baryonic effects.

Unified Astronomy Thesaurus concepts: N-body simulations (1083); Cosmological parameters from large-scale structure (340); Redshift surveys (1378)

1. Introduction

The accelerated expansion of the universe has been one of the most profound mysteries in astronomy and physics since observations confirmed it through the redshift–distance relation of SNe Ia (Riess et al. 1998; Perlmutter et al. 1999). So far, the ΛCDM model gives the best description for these observations, although it involves several theoretical difficulties related to the smallness and fine-tuning of Λ, the exotic form of the energy in the universe (Frieman et al. 2008; Weinberg et al. 2013). Another conceptual possibility for the apparent accelerated expansion is that general relativity, on which the ΛCDM model is built, may not be correct on cosmological scales. This idea gave rise to the modified gravity theories, which realize the same redshift–distance relation as that of the ΛCDM model without relying on dark energy but predict a different gravitational growth history of the matter content of the universe (Joyce et al. 2016; Koyama 2016). Discriminating between the dark energy and modified gravity scenarios is essential to better understand the origin and history of our universe.

The redshift-space distortion (RSD) is the phenomenon that the observed distribution of galaxies is distorted from the real one due to the noncosmological redshift caused by galaxy peculiar motion (Kaiser 1987; Hamilton 1998). It affects the statistical properties of galaxy clustering, such as the two-point correlation function (2pCF) and the power spectrum, making the line-of-sight direction a special one. As the galaxy peculiar velocity field is governed by the gravity law and background cosmological parameters, the anisotropy of the galaxy 2pCF is sensitive to the change of cosmological models, making RSD a powerful cosmological probe (Weinberg et al. 2013). Since the galaxy catalog used in an RSD analysis can also be used for other cosmological probes, such as large-scale structure topology (Park & Kim 2010; Appleby et al. 2018), richness and size distributions of structures (Hwang et al. 2016), baryon acoustic oscillations, and the Alcock–Paczynski test (Reid et al. 2012; Li et al. 2016; Sánchez et al. 2017), there have been a variety of galaxy redshift surveys (Sloan Digital Sky Survey (SDSS), York et al. 2000; HectoMAP, Geller et al. 2011; BOSS, Dawson et al. 2013; 6dF, Jones et al. 2005; WiggleZ, Drinkwater et al. 2010; VIPERS, Guzzo et al. 2014; FastSound, Tonegawa et al. 2015; eBOSS, Dawson et al. 2016). There are also further large upcoming surveys (PFS, Takada et al. 2014; DESI, DESI Collaboration et al. 2016; WFIRST, Spergel et al. 2015).

The large-scale RSD is caused by the infall motion of galaxies during the structure formation, and it has been detected by various redshift surveys, giving strong cosmological constraints on the growth rate of the large-scale structure $f = d\ln D/d\ln a$ (Hawkins et al. 2003; Guzzo et al. 2008; Blake et al. 2011; Beutler et al. 2012, 2014; de la Torre et al. 2013; Samushia et al. 2013;

Okumura et al. 2016; Icaza-Lizaola et al. 2020), where D is the growth factor and a is the scale factor of the universe, with $a = 1$ at the present epoch. On the other hand, the small-scale RSD, called the Finger-of-God (FoG) effect (Jackson 1972; Sargent & Turner 1977), is caused by the orbital motion of galaxies inside galaxy groups and clusters. It has not been studied as much as the large-scale RSD but has rich cosmological information because different cosmological parameters lead to different halo mass functions and virialized velocities (Marzke et al. 1995). The difficulty in using the small-scale RSD lies in the theoretical prediction of the density and velocity field in highly nonlinear scales. We cannot rely on the perturbation theory that is valid down to the mildly nonlinear regime (Taruya et al. 2010) because the FoG effect takes place in almost or completely relaxed objects. There have been attempts to understand the pairwise velocity of galaxies, which is an essential ingredient for the small-scale redshift-space 2pCF (Sheth 1996; Juszkiewicz et al. 1998; Tinker 2007; Bianchi et al. 2016; Kuruvilla & Porciani 2018). While they gave illuminating insights on why the pairwise velocity distribution has the shape of what we observe, their models typically include free parameters that may depend on cosmological models and are not easy to derive from the first principles thus far. Nevertheless, because of the small statistical uncertainty, the use of small-scale clustering will significantly enhance our constraining power from the limited size of observational data sets.

While the analytic prescription of the nonlinear structure formation is a timely topic itself (Tinker 2007), N-body simulations can serve as an alternative to small-scale cosmology studies (DeRose et al. 2019). In this study, we use the Multiverse Simulation (Shin et al. 2017; Park et al. 2019; Hong et al. 2020 for scientific applications), the Horizon Run 4 Simulation (Kim et al. 2015), and a physically motivated galaxy assigning scheme (Hong et al. 2016) to mock the galaxy distributions in redshift space for different matter density parameters Ω_m, satellite velocity bias parameters b_v^s, and merger timescale parameters α. The galaxy–halo correspondence in our model has more physical meaning than the halo occupation distribution (HOD) approach. Reid et al. (2014) adopted the HOD approach and successfully explained the redshift-space clustering of the BOSS CMASS data, obtaining a 2.5% constraint of the growth rate, which clearly proved the usefulness the small-scale clustering information. Although it is the standard method to connect galaxies and halos, the HOD has several issues to examine carefully. The HOD prescribes the probability of a halo of mass M having N galaxies, $P(N|M)$, with typically five parameters and specific functional forms. However, there is no particular reason for the number of parameters and functions. The number N may also depend on secondary parameters, such as halo age and galaxy assembly history (Wang et al. 2013; Montero-Dorta et al. 2017; Beltz-Mohrmann et al. 2020). By contrast, our galaxy–halo corresponding scheme traces the merger tree and automatically places galaxies into subhalos, which avoids the theoretical uncertainties. We constrain the matter density parameter Ω_m, as well as the velocity bias parameter for satellite galaxies b_v^s and the merger timescale parameter α, by simultaneously matching the measurements of the projected correlation function and the multipole moments of the 2pCF between simulation and observation. We also define the "strength" of FoG and show that adding it helps us to constrain our model parameters more strongly.

The structure of this paper is as follows. In Section 2, we describe the simulation and observational data that we use. In Section 3, we measure the correlation functions and covariance matrix. We also quantify the FoG strength to extract cosmological information from the small-scale 2pCF. In Section 4, we show our constraints on the parameters of our model, followed by discussions in Section 5. Finally, we summarize our study in Section 6.

2. Data and Models

2.1. The KIAS-VAGC Catalog

We use the Korea Institute for Advanced Study Value-Added Galaxy Catalog (KIAS-VAGC; Choi et al. 2010) as observational data. This catalog is based on the New York University Value-Added Galaxy Catalog (Blanton et al. 2005) as part of the SDSS Data Release 7 (DR7; Abazajian et al. 2009) but supplements missing redshifts with other galaxy redshift catalogs for better redshift completeness. The KIAS-VAGC covers $\sim$8000 deg^2 on the celestial plane and contains 593,514 redshifts of the SDSS main galaxies in an r-band Petrosian magnitude of $10.0 < m_r < 17.6$. The supplementation increased the area with completeness higher than 0.97 from 39.8% to 54.3%. There are still missing redshifts even after this supplementation, which is mainly caused by the fiber collision effect and poor observing conditions. The fiber collision rate is estimated to be $\sim$5% but lower in the overlapping regions. In the KIAS-VAGC catalog, these galaxies are marked and given the redshifts of the nearest galaxy on the celestial plane.

We use the volume-limited sample "D5" with a redshift cut $0.025 < z < 0.10713$ and an r-band absolute magnitude cut $M_r < -20.02 + 5\log h$, as defined in Park & Choi (2009). The number density is 0.063 $(h^{-1}\,\mathrm{Mpc})^{-3}$, and the median redshift is 0.083. Also, we restrict the sample to the largest area that satisfies $-65.^\circ0 < \lambda < 65.^\circ0$ and $-37.^\circ0 < \eta < 43.^\circ0$, where λ and η are the SDSS survey coordinates. The KIAS-VAGC also provides the survey mask, which indicates the spectroscopic completeness in each 0.025×0.025 deg^2 patch in the survey area. To avoid bad observing conditions and shot noise, we only use the region where the completeness is above 0.8. All galaxies in the valid region are assigned the weight as the inverse of the completeness. Some of the target galaxies are not allocated fibers due to the mechanical limitation of the minimum separation of two galaxies on the sky. This is called the fiber collision effect; it occurs on small scales ($\sim$0.1 Mpc) and potentially weakens the FoG effect. If a spectroscopic target cannot be allotted a fiber, the redshift of the nearest neighbor (NN) galaxy is given to the galaxy. The validity of this approach will be discussed in Appendix C.

The random catalog is needed to measure the correlation function. Since we are using a volume-limited subsample, we make random catalogs as the uniform distribution in a comoving volume. The angular completeness mask is then applied after the conversion from (X, Y, Z) to (λ, η) to discard points on the region of completeness <0.8. The size of the random catalog is $\sim$30 times larger than the corresponding data.

2.2. The Multiverse Simulation

The Multiverse Simulation is a collection of large-volume cosmological N-body simulations with different cosmological parameters (Shin et al. 2017; Park et al. 2019). There are five realizations that have different matter density Ω_m and equation of state of the dark energy w—$(\Omega_m, w) = (0.21, -1.0)$, $(0.26, -1.0)$, $(0.31, -1.0)$, $(0.26, -0.5)$, and $(0.26, -1.5)$—keeping $\Omega_m + \Omega_\Lambda = 1$, while other parameters are fixed to the Wilkinson Microwave Anisotropy Probe (WMAP) 5 yr result (Dunkley et al. 2009): $\Omega_b = 0.044$, $n = 0.96$, $H_0 = 72\,\mathrm{km\,s^{-1}\,Mpc^{-1}}$, and $\sigma_8 = 0.79$. We use the first three simulated models out of five because the change in w will not be important for the clustering properties on the scales that we are interested in. The comoving box size is 1024^3 $(h^{-1}\,\mathrm{Mpc})^3$, and 2048^3 dark matter (DM) particles are evolved inside, which leads to a particle mass of $9 \times 10^9(\Omega_m/0.26)\,M_\odot$. The starting redshift is $z = 99$, and 1980 snapshots are saved until $z = 0$. Halos are identified through a friends-of-friends (Davis et al. 1985) algorithm with a commonly used linking length of $b = 0.2$. The minimum number of particles to be qualified as a halo is 30, which means a minimum halo mass of $2.7 \times 10^{11}(\Omega_m/0.26)\,M_\odot$. Halos in each snapshot are searched for the most bound particle (MBP), which is located at the lowest gravitational potential. The merger tree is built by tracking the merger trajectories of MBPs.

Simulated galaxies are assigned to the DM halos by the MBP–galaxy correspondence approach as described by Hong et al. (2016). All MBPs marked in the merger tree are regarded as galaxy proxies, and physical properties of MBPs such as mass, position, and velocity are allocated to the modeled galaxies. If a merger occurs, the roles of host and satellite are assigned to each MBP according to the mass of the halos in the previous time step. Then, the satellites are monitored to determine their fates (i.e., escape from the gravitational potential of its host or tidally disrupted) according to the modified version of the merger timescale of Jiang et al. (2008),

$$\frac{t_{\mathrm{merge}}}{t_{\mathrm{dyn}}} = \frac{(0.94\epsilon^{0.60} + 0.60)/0.86}{\ln[1 + (M_{\mathrm{host}}/M_{\mathrm{sat}})]}\left(\frac{M_{\mathrm{host}}}{M_{\mathrm{sat}}}\right)^{\alpha}, \tag{1}$$

where ϵ, M_{host}, and M_{sat} are the circularity of the satellite's orbit and the mass of the host and satellite halos, and t_{dyn} is the dynamical timescale

$$t_{\mathrm{dyn}} = \frac{R_{\mathrm{vir}}}{V_{\mathrm{vir}}}, \tag{2}$$

with R_{vir} and V_{vir} being the virial radius and circular velocity, respectively. The α parameter is the only fitting parameter that controls the merger timescale of satellites. Increasing α, on average, increases the number of satellite galaxies and will enhance the overall amplitude of correlation functions, as well as the FoG effect. Due to the limited computational resource, only three implementations for $\alpha = 1.0$, 1.5, and 2.0 are carried out. In Section 4, we will see that $\alpha = 1.5$ results in the best agreement between simulation and observation for the projected 2pCF of the volume-limited samples of galaxies with r-band absolute magnitudes of $M_r < -20$. Therefore, we use $\alpha = 1.5$ in this study as a fiducial model, but we also show some results and comparisons with other α values.

2.3. The Horizon Run 4 Simulation

The Horizon Run Simulations (Kim et al. 2009, 2015) are large cosmological N-body simulations run by the KIAS. To date, there are four realizations (Runs 1, 2, 3, and 4) with different box sizes and particle numbers. The Horizon Run 4 (HR4) has evolved 6300^3 particles with a mass of $3.0 \times 10^9\,M_\odot$ in a $3150\,h^{-1}$ Mpc long cubic box. The HR4 is 27 times larger than the Multiverse Simulation, allowing us to estimate the covariance matrix more accurately. The adopted cosmological parameters are the same as those of the $(\Omega_m, w) = (0.26, -1.0)$ case of the Multiverse Simulation. While we use the Multiverse Simulation to investigate the small-scale clustering property for different cosmological parameters, we use the HR4 simulation to calculate the covariance matrix and test systematics, including the fiber collision effect. The galaxy assignment was performed in an identical way to those of the Multiverse Simulation. To estimate the covariance matrix, we divide the HR4 simulation box into $5 \times 9 \times 5 = 405$ subcubes. The choice of the number is because of the geometry of the SDSS main galaxy survey volume, whose length in one dimension is longer than those of the other two. In each subcube, an origin is set, and the galaxy positions are converted into (R.A., decl., z). Then, the RSD effect is applied using the line-of-sight velocity of galaxies (see the next subsection). We set $\alpha = 1.5$ and the velocity bias parameter $b_v^s = 1$ for the calculation of the covariance matrix. The covariance matrix may be a function of these parameters, but we will ignore it. The parameter fitting in Section 4.3 is performed using the covariance matrix obtained here, and all error bars in the measurements of Figures 3, 4, 5, and 7 are the square root of the diagonal elements of the covariance matrix.

2.4. The RSD and Velocity Bias

While the mock galaxy distribution is simulated in real space, the observed galaxy clustering statistics come from the redshift-space distribution. Thus, we need to apply the RSD effect to the simulation data.

The RSD alters the apparent galaxy position along the line of sight due to the peculiar motion in the radial direction (Hamilton 1998). As we take the third axis of the simulation as the line-of-sight direction, the positions are modified as

$$x_3^g \mapsto x_3^g + v_3^g/aH, \tag{3}$$

where $\boldsymbol{x}^{\mathrm{g}} = (x_1^g, x_2^g, x_3^g)$ and $\boldsymbol{v}^{\mathrm{g}} = (v_1^g, v_2^g, v_3^g)$ are the comoving position and peculiar velocity of a galaxy, and H is the Hubble parameter at redshift z. The periodic boundary condition is applied if the modified position exceeds the boundary of the simulation box. For the first term of the right-hand side, we use the MBP positions as a proxy of the galaxy positions.

Recently, it has been argued, based on the observations and simulations (Munari et al. 2013; Wu et al. 2013; Guo et al. 2015; Ye et al. 2017), that the galaxy velocity distribution may not be the same as that of DM inside halos. Guo et al. (2015) found that the speed of satellite galaxies inside halos was lower (typically ∼80%) than the velocity dispersion of the DM, σ_v. Possible origins of such a discrepancy include statistical bias, dynamical friction, galaxy interactions, and hydrodynamic effects. Also, central galaxies may not be at rest at halo centers, with a velocity dispersion of $\sim 0.3\sigma_v$. Given that, we

parameterize the satellite velocity bias by a single parameter b_v^s,

$$\boldsymbol{v}^{\rm g} - \boldsymbol{v}^{\rm h} = b_v^s(\boldsymbol{v}^{\rm MBP} - \boldsymbol{v}^{\rm h}), \quad (4)$$

where $\boldsymbol{v}^{\rm MBP}$ and $\boldsymbol{v}^{\rm h}$ are the MBP velocity of the galaxy and the host halo velocity, respectively. The host halo velocity is defined as the average velocity of the member particles. Equation (4) means that, in the rest frame of the hosting halo, the velocity of the visible part of the galaxies is different from that of all of the matter (represented by MBPs) by a factor of b_v^s. Note that our definition of the velocity bias is different from that of Guo et al. (2015). They referred to α_v^s as the rms velocity of satellites relative to the velocity dispersion of DM of their hosts, $\langle|\boldsymbol{v}^{\rm g} - \boldsymbol{v}^{\rm h}|\rangle = \alpha_v^s\sigma_v$, and used α_v^s to fit to the SDSS volume-limited sample. Therefore, their α_v^s includes all factors that cause the velocity difference between the baryonic component of galaxies and DM inside halos. Some of the factors for the velocity bias are hydrodynamic, and others are gravitational. Because the MBP–galaxy assignment approach naturally includes all gravitational effects, the difference between $|\boldsymbol{v}^{\rm MBP} - \boldsymbol{v}^{\rm h}|$ and σ_v will reflect these effects. As in Equation (4), our b_v^s is defined as the difference between the visible component and all of the matter of the galaxy represented by MBPs inside the halo; hence, b_v^s will indicate only the baryonic effects that cause the velocity bias. Combining α_v^s and b_v^s will tell us to what degree each origin contributes to the velocity bias. Figure 1 shows the relation between the $|\boldsymbol{v}^{\rm MBP} - \boldsymbol{v}^{\rm h}|$ of centrals or satellites and σ_v of DM halos in the case of $\Omega_m = 0.26$. The colored lines show central 68th and 95th percentile intervals, which are obtained by quantile regression using B-splines (Ng & Maechler 2020). The galaxy density is set to be similar to the observation data we use. The median of $|\boldsymbol{v}^{\rm MBP} - \boldsymbol{v}^{\rm h}|/\sigma_{\rm v}$ is 0.94 for satellite galaxies; the center of mass of satellite galaxies moves slightly slower than the velocity dispersion of DM inside the hosting halo.

One might wonder that the trajectories of MBPs and galaxies may diverge (i.e., the position of a galaxy in the next time step would be inconsistent with the corresponding MBP) if MBPs and galaxies have different velocities. Ideally, if the MBP represents the galaxy position and velocity correctly over cosmic time, b_v has to be 1. Our logic behind Equation (4) is that we try to absorb the secondary effects that may cause the velocity difference between the *N*-body simulation and the real observation, in response to the results of previous studies. Although we expect that b_v should be close to 1 even if such effects are present, a significant deviation from $b_v \sim 1$, if detected, would indicate an incompleteness of using *N*-body simulations to fit the observational data on small scales.

Considering that the central galaxies have spent a relatively longer time inside clusters and should be better relaxed ($\boldsymbol{v}^{\rm g} \sim \boldsymbol{v}^{\rm MBP}$), the MBP velocity would be a good representative of the velocity of the baryonic part of the central galaxy. Therefore, instead of making further sophistication, we use the velocity of the central MBP as the central galaxy velocity for most of our paper. As seen in Figure 1, the MBP velocity is in the range of 30%–50% of σ_v. This compares with the estimate on $\alpha_v^s \sim 0.3$ in Guo et al. (2015). In Appendix B, we will present the result obtained by modifying the MBP velocity for central galaxies. Also, note that the velocity bias can be a function of galaxy properties such as age and mass, and studying the dependence of the velocity bias in detail would help us to understand the dynamical aspects of the evolution of galaxies, but we will only use a single parameter b_v^s in this work.

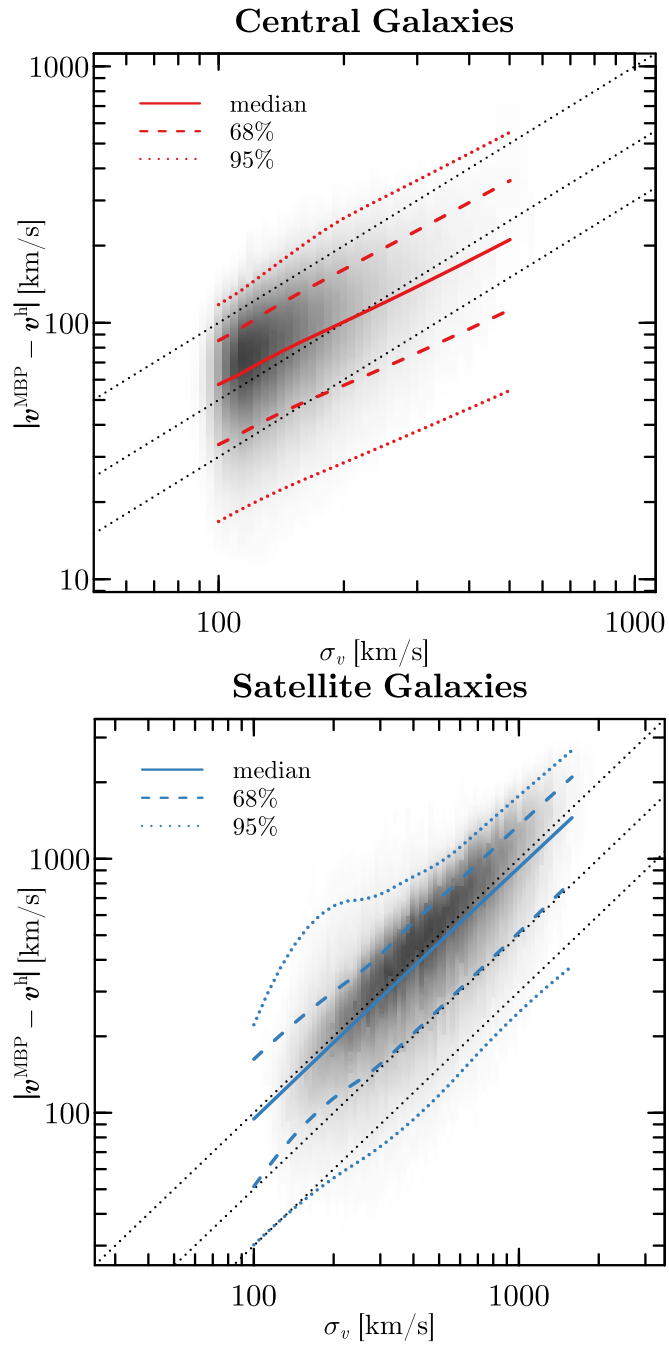

Figure 1. The MBP's velocity in the halo frame vs. the velocity dispersion of the DM halo particles. The top panel is for central galaxies and bottom panel for satellite galaxies. The colored lines indicate the median and the 68th and 95th percentile ranges. The black dotted lines correspond to $|\boldsymbol{v}^{\rm MBP} - \boldsymbol{v}^{\rm h}|/\sigma_v = 1$, 0.5, and 0.3. The model parameters are fixed to be $\Omega_m = 0.26$ and $\alpha = 1.5$.

In summary, our model parameters are

1. matter density parameter $0.15 < \Omega_m < 0.37$,
2. merger timescale parameter $\alpha = 1.5$, and
3. satellite velocity bias $0.3 < b_v^s < 1.7$.

3. Measurements

3.1. Multipole Moments of the Correlation Function

As a statistical quantity of the redshift-space clustering, we use the multipole moments of the correlation function. First, the 2pCF is given by the Landy–Szalay estimator (Landy & Szalay 1993),

$$\xi(\boldsymbol{s}) = \frac{\mathrm{DD} - 2\mathrm{DR} + \mathrm{RR}}{\mathrm{RR}}, \tag{5}$$

where DD, DR, and RR are the counts of galaxy–galaxy, galaxy–random, and random–random pairs, respectively. The vector $\boldsymbol{s}$ can be $\boldsymbol{s} = (r_p, r_\pi)$ or (s, μ), where r_p and r_π are the transverse and parallel components of the separation of galaxy pairs, while $s = |\boldsymbol{s}|$ and $\mu = r_\pi/s$.

The multipole moments are calculated as

$$\xi_l(s) = \frac{2l+1}{2}\int_{-1}^{1} \xi(s, \mu) L_l(\mu) d\mu, \tag{6}$$

where $L_l(\mu)$ is the Legendre polynomial of the lth degree. Because the moments of odd numbers vanish due to the symmetry[7] and higher-order multipoles become less informative due to higher measurement noises, we use only $l = 0$ (monopole), 2 (quadrupole), and 4 (hexadecapole): $L_0 = 1$, $L_2(\mu) = \frac{1}{2}(3\mu^2 - 1)$, and $L_4(\mu) = \frac{1}{8}(35\mu^4 – 30\mu^2 + 3)$. Because of the Kaiser effect, ξ_0 is enhanced and ξ_2 becomes negative in redshift space on scales larger than $\gtrsim 10\ h^{-1}$ Mpc, while the opposite holds at cluster scales. We use a bin size of $\Delta\mu = 0.05$ and eight logarithmic bins from $s = 1.43$ to $30\ h^{-1}$ Mpc.

3.2. The Projected Correlation Function

The projected correlation function is obtained by the integration along the line of sight,

$$w(r_p) = \int_{-r_{\pi,\max}}^{r_{\pi,\max}} \xi(r_p, r_\pi) dr_\pi. \tag{7}$$

We set $r_{\pi,\max} = 40\ h^{-1}$ Mpc and confirm that larger $r_{\pi,\max}$ hardly changes $w(r_p)$. The projected correlation function is a measure of clustering in real space, because the line-of-sight projection eliminates the RSD effect, whereas the multipole moments are the redshift-space quantities. It will be shown that using the projected correlation function can break the degeneracies between the cosmological matter density parameter (Ω_m), the merger timescale parameter (α), and the velocity bias (b_v^s) that are not fully broken by using multipoles only.

3.3. The FoG Ratio

The multipole moments of the correlation function are measures of the RSD effects, but they are also affected by the change of the overall clustering amplitude, which can vary due to the cosmic variance and other systematics. Thus, we try to extract pure RSD information that is independent of the amplitude. We use a measure of the strength of the RSD effects as follows,

$$R_{|\xi=3} = \frac{r_{\pi|\xi=3}}{r_{p|\xi=3}}, \tag{8}$$

which is the ratio of the separations along and across the line of sight from a point close to the origin to locations where the correlation function drops to 3. The ratio for different threshold values can be defined likewise. The schematic image is given by Figure 2. By taking a ratio, the cosmic variance in density fluctuations is expected to cancel out, giving a clean measurement of the strength of the FoG effect.

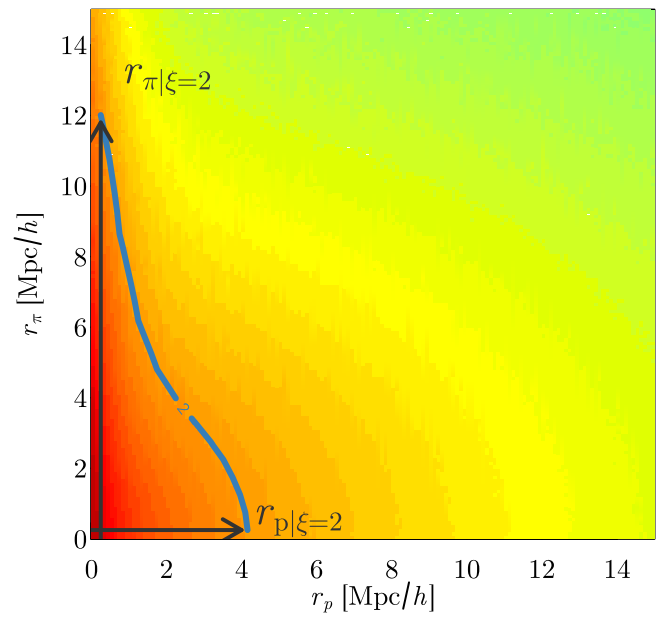

Figure 2. Conceptual image of the FoG ratio. The colored image is the redshift-space correlation function of galaxies taken from the Multiverse Simulation with $\Omega_m = 0.26$. The blue line shows the contour at the level of $\xi(r_p, r_\pi) = 2$. The arrows correspond to the numerator and denominator of Equation (8).

We calculate the correlation functions for the Multiverse Simulation and KIAS-VAGC catalogs, covering $0.1\ h^{-1}\ \mathrm{Mpc} < r_p < 30\ h^{-1}$ Mpc and $0.1\ h^{-1}\ \mathrm{Mpc} < r_\pi < 30\ h^{-1}$ Mpc with 15×15 logarithmic bins. Then, we take the fourth-smallest bins ($\sim 0.4\ h^{-1}$ Mpc), $\xi(0.4, r_\pi)$ and $\xi(r_p, 0.4)$, to locate the point at which the correlation function becomes a certain threshold value. The scale $\sim 0.4 h^{-1}$ Mpc is chosen to be sufficiently small to capture the FoG feature while keeping the statistical uncertainty small with enough pair counts.

3.4. The Covariance Matrix

The covariance matrix is necessary for evaluating the goodness of fit. We use the mock galaxy catalogs created from the HR4 data, which has a 3150^3 $(h^{-1}\ \mathrm{Mpc})^3$ volume. Using the 405 mock catalogs from HR4, we have found that the distributions of our observables follow the Gaussian distribution. For each data point, we compared the distribution of mock values to the Gaussian distribution of the same mean and variance using the Kolmogorov–Smirnov test for the null hypothesis of the mocks following Gaussian. The resulting p-values are 0.4–0.9, indicating no evidence for non-Gaussian distributions. Therefore, we can use the standard χ^2 statistics to evaluate the goodness of fit.

[7] The relativistic effect can cause asymmetry by breaking the symmetry along the line of sight (Alam et al. 2017), but we do not consider it because the effect is much smaller than RSD.

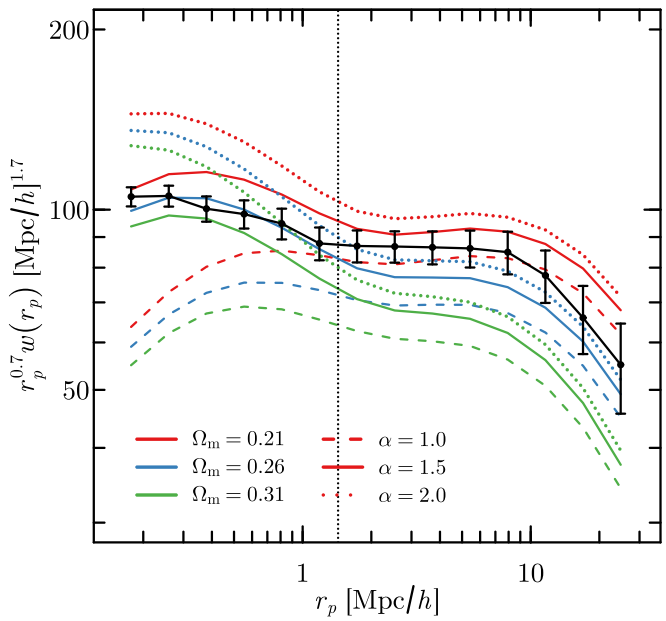

Figure 3. Projected correlation function $w(r_p)$ for different α and Ω_m. The values are multiplied by $r_p^{0.7}$ for a visual purpose. The black line represents the SDSS observation data, while the colored lines are obtained from the Multiverse Simulation for corresponding Ω_m values. Different line types are for different merger timescales α. The dotted vertical line indicates the minimum scale for our fittings.

We adopt the χ^2 statistics to constrain the model parameters,

$$\chi^2 = [\boldsymbol{X}^{\rm obs} - \boldsymbol{X}^{\rm th}(\boldsymbol{\theta})]^T \mathbb{C}^{-1} [\boldsymbol{X}^{\rm obs} - \boldsymbol{X}^{\rm th}(\boldsymbol{\theta})], \quad (9)$$

where $\boldsymbol{X}$ is the data vector, $\mathbb{C}$ is the covariance matrix corresponding to $\boldsymbol{X}$, and the superscripts represent the observation and model prediction for parameters $\boldsymbol{\theta} = (\Omega_m, \alpha, b_v^s)$, respectively. For example, if we use ξ_0 and ξ_2 for the fitting, $\boldsymbol{X}$ will be a vector of $8 \times 2 = 16$ elements, and $\mathbb{C}$ will be a 16×16 sized matrix. We apply the correction of Hartlap et al. (2007) to the covariance matrix to account for the underestimation of the covariance matrix due to the finite number of realizations. Because we use 405 mock catalogs, the correction factor is 1.02–1.10, depending on the size of the data vector. Also, we multiply the covariance matrix by $(1 + V_{\rm obs}/V_{\rm simu}) = 1.02$ to account for the uncertainty arising from the finite volume of the simulation box $V_{\rm simu}$ used to model the observation of volume $V_{\rm obs}$ (Zheng & Guo 2016).

4. Results

4.1. The Correlation Functions

The projected correlation function is shown in Figure 3. Different colors correspond to different Ω_m, while different line types correspond to different α. Because we fix the overall density perturbation amplitude, $\sigma_8 = 0.79$, increasing Ω_m shifts the matter–radiation equality, resulting in weaker correlations at the scales we are interested in. An increase in α enhances the overall amplitude due to the increased number of satellite galaxies. The change is more drastic on small scales than large scales, implying that the small-scale information is useful to discriminate different α scenarios, in turn giving a better constraint on Ω_m. Also, it should be mentioned that the measurement error is small on smaller scales due to the larger number of pairs. While $\alpha = 1.0$ and 2.0 fail to reproduce the observation, the most probable value of α seems to be around 1.5. Note that $w(r_p)$ does not depend on b_v^s because $w(r_p)$ is a real-space quantity and not affected by RSD.

Figure 4 shows the dependence of multipole moments on Ω_m and b_v^s. Different panels are for different multipole moments. The dependence of multipoles on Ω_m is complicated. Both the Kaiser effect and FoG become stronger in a higher-Ω_m universe (Feldman et al. 2003; Linder 2005); thus, ξ_0 should be suppressed (enhanced) at small (large) scales, which is not the case at relatively large scales ($\sim 20\,h^{-1}$ Mpc). This contradiction is caused by the weaker real-space clustering for higher Ω_m, as we saw in Figure 3, which is not fully compensated by the stronger Kaiser effect. For ξ_2, the positive (negative) sign indicates the elongated (squashed) feature. On larger scales, where the Kaiser effect dominates, $\xi_2 < 0$, and on small scales, where the FoG does, $\xi_2 > 0$. Again, a contradictory trend is seen in the middle panel of Figure 4, which we attribute to the overall amplitude of the real-space clustering. Another notable feature is the position of the peak of ξ_2. If we increase b_v^s, the peak shifts toward larger s. This is because large b_v^s leads to a strong FoG effect, increasing the transition scale from the FoG to the Kaiser effect. The position of the peak supports b_v^s close to 1.0.

4.2. The FoG Ratio

Figure 5 shows $R_{|\xi}$ for different Ω_m and b_v^s as a function of the threshold value. Here $R_{|\xi}$ is smaller for lower thresholds because lower thresholds correspond to larger scales where the FoG effect is less dominant and the Kaiser effect becomes more effective, which reduces $R_{|\xi}$. A strong degeneracy between Ω_m and b_v^s is seen. As Ω_m becomes higher, both the population of massive halos and the virialized velocity become higher too (Marzke et al. 1995; Vikhlinin et al. 2009), which leads to the stronger FoG effect. Also, a higher velocity bias means a higher galaxy motion inside clusters and thus a stronger FoG. Within the error bars of the observation, both $(\Omega_m, b_v^s) = (0.21, 1.0)$ and (0.31, 0.7) reproduce the observed FoG ratio reasonably well. If we had complete knowledge of α and b_v^s, the FoG ratios would give a constraint of $\Delta\Omega_m \sim 0.02$ with our data. However, if we allow these to vary, using only the FoG ratio is insufficient to obtain a meaningful constraint on Ω_m.

4.3. The Fitting

Next, let us see how well the fittings work. The peak position of the middle panel of Figure 4 tells us that $b_v^s \sim 1.0$ will give the best fit. Then, we notice that $\Omega_m \sim 0.26$ is preferred in the top panel by comparing the observation with the solid colored lines. Figure 6 shows the probability distribution of Ω_m and b_v^s based on the χ^2 statistics for $\alpha = 1.5$. Because we only have three Ω_m realizations, any statistical quantity (ξ_l, $w(r_p)$, and $R_{|\xi}$) for other Ω_m is obtained by interpolation. Different lines correspond to what type(s) of information is (are) used to fit. The bold red contour is the combined result obtained by fitting to the monopole, quadrupole, and hexadecapole moments and the projected 2pCF. The thin blue contour is from the FoG ratio, and the bold blue contour is the combination of these two. Note that the projected 2pCF is the real-space quantity; therefore, it cannot constrain b_v^s but can indirectly contribute to better determining b_v^s by constraining Ω_m. All contours overlap one another in the $\alpha = 1.5$ case. This means that $\alpha = 1.5$ can explain all measurements simultaneously, supporting the

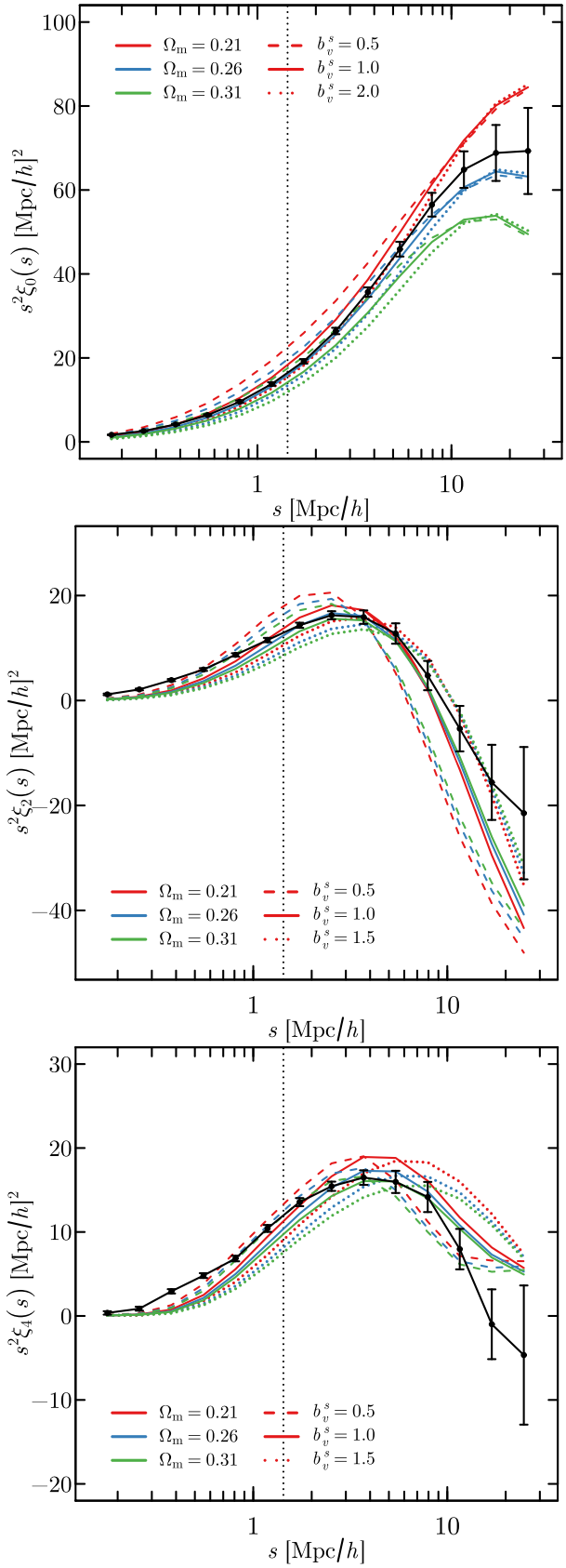

Figure 4. Multipole moments ξ_l ($l = 0$, 2, and 4 for the top, middle, and bottom panels, respectively). Black lines represent the observation data, while colored lines are obtained from the Multiverse Simulation for corresponding Ω_m values. Different line types are for different satellite velocity bias b_v^s. The α parameter is fixed to be 1.5.

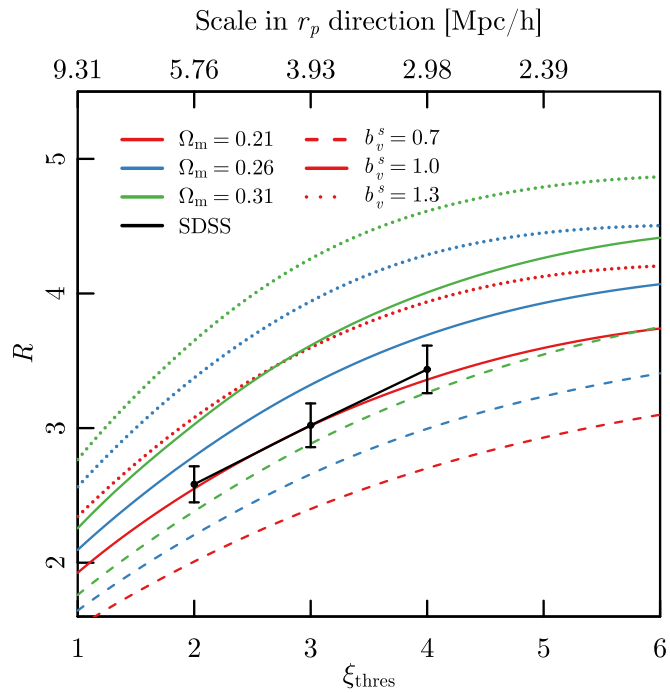

Figure 5. The FoG ratio R as a function of the correlation function threshold level. The colored lines are obtained from the Multiverse Simulation for different Ω_m, while the black line is from the SDSS observation. Different line styles indicate different satellite velocity bias b_v^s. The α parameter is fixed to be 1.5. For reference, approximate scales for corresponding threshold levels are shown on the top axis.

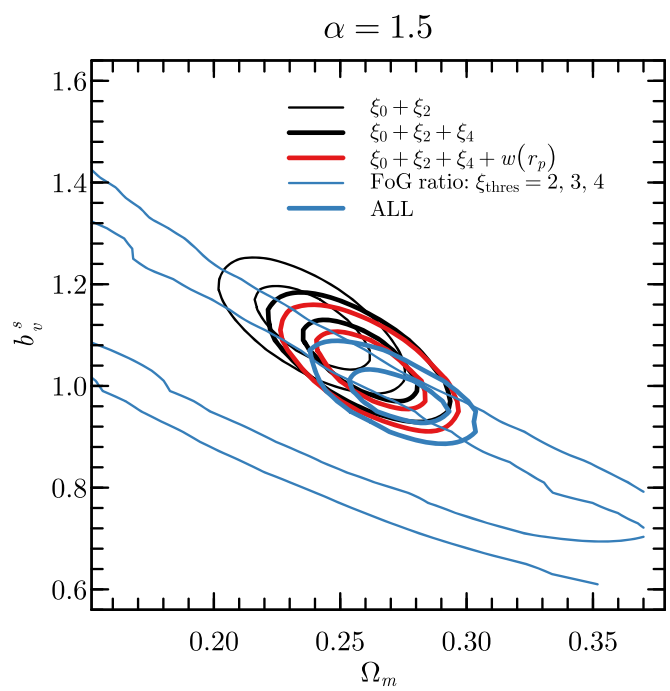

Figure 6. Constraints on (Ω_m, b_v^s) from the χ^2 analysis for the case $\alpha = 1.5$. The contours show 68% and 95% confidence levels. The constraints are obtained by using different combinations of the measurements as given in different line types and colors.

validity of our modeling of the galaxy clustering. The best-fit values for the $\xi_0 + \xi_2 + \xi_4 + w(r_p)$ case are $(\Omega_m, b_v^s) = (0.262 \pm 0.014, 1.032 \pm 0.051)$. As seen in Figure 6, including ξ_4 and $w(r_p)$ does not change the best fit within the

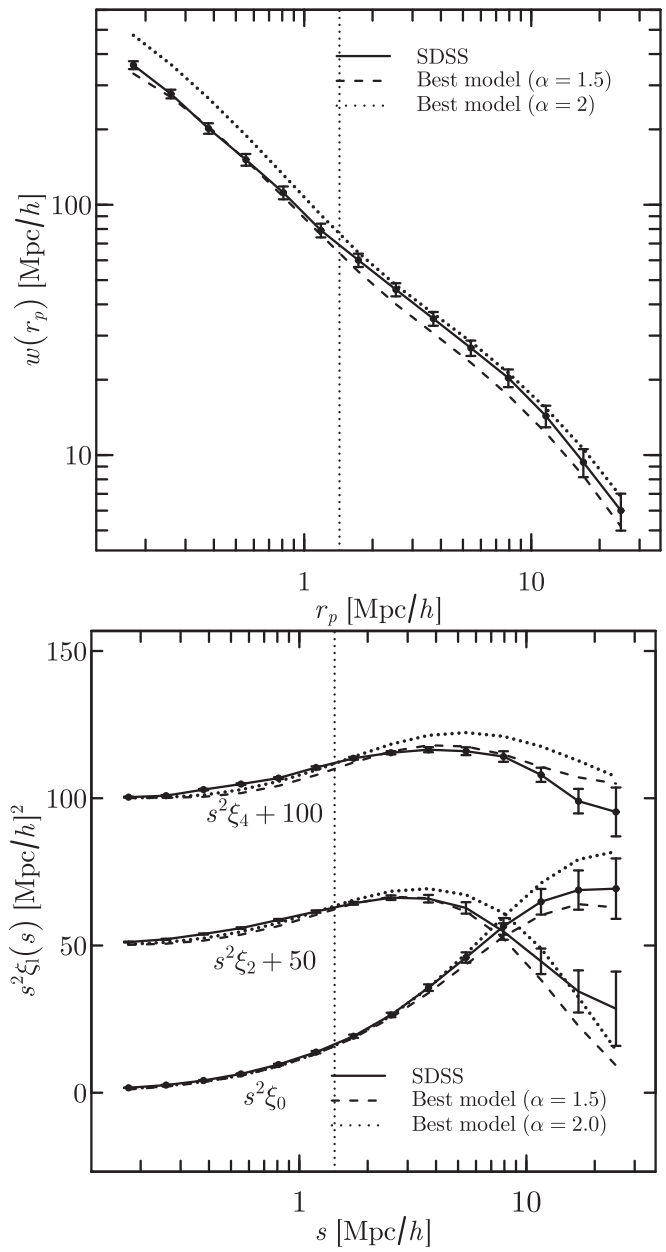

Figure 7. Projected correlation function (top) and multipole moments (bottom). The solid lines are the measurements from the SDSS. The dashed line is the best model for $\alpha = 1.5$, obtained from the combination of $w(r_p)$, ξ_0, ξ_2, and ξ_4 (bold red contour in Figure 6). The dotted line is similar to the dashed line but for the $\alpha = 2.0$ model. For the log-likelihood of parameters for $\alpha = 2.0$, see Figure 9. The vertical lines show the minimum scale we used for the fittings.

statistical uncertainty or tighten the constraint significantly. However, note that $w(r_p)$ has given a good constraint on α, as seen in Figure 3. Adding the FoG ratio yields $(\Omega_m, b_v^s) = (0.272 \pm 0.013, 0.982 \pm 0.040)$.

Figure 7 gives a comparison between the observation and the best-fit models for $\alpha = 1.5$ and 2.0. The fitting procedure for $\alpha = 2.0$ is identical to that for $\alpha = 1.5$, except that we have used $\alpha = 2.0$ in Equation (1) to produce the simulated galaxies in the Multiverse Simulation. The top panel shows the projected 2pCF, while the bottom panel shows the multipoles. Except for a weak deviation ($\sim 1\sigma$) at $s > 10\,h^{-1}$ Mpc, our $\alpha = 1.5$ model reproduces $w(r_p)$, ξ_0, and ξ_2 very well. A moderate deviation is seen at $s \sim 1\,h^{-1}$ Mpc of ξ_4, which

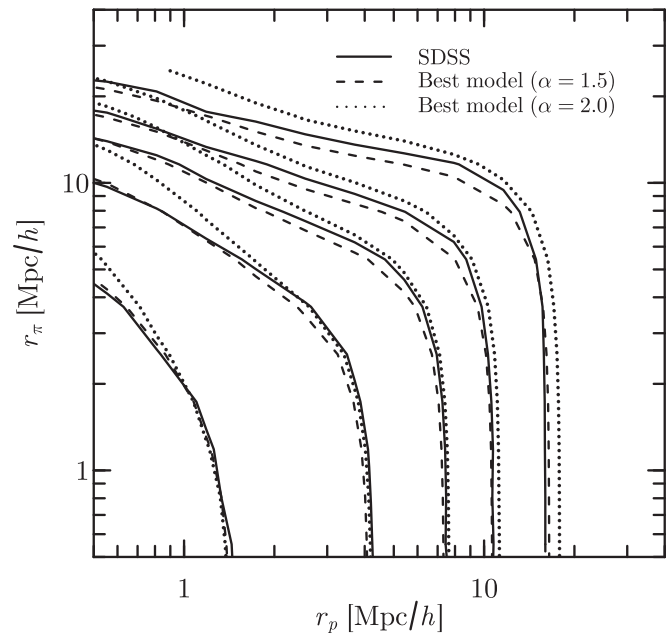

Figure 8. The 2D correlation function $\xi(r_p, r_\pi)$. The contour levels are 6, 2, 1, 0.6, and 0.3. Axes are expressed in a logarithmic scale to emphasize the small-scale part. The solid lines are obtained from the measurements of the SDSS data. The dashed lines are the best model for $\alpha = 1.5$, obtained from the combination of $w(r_p)$, ξ_0, ξ_2, and ξ_4 (bold red contour in Figure 6). The dotted lines are similar to the dashed lines but for the $\alpha = 2.0$ model. For the log-likelihood of parameters for $\alpha = 2.0$, see Figure 9.

mainly contributes to our χ^2 (see Appendix A for detailed discussions). Also, we can see a good fit of $w(r_p)$ at $r_p < 1\,h^{-1}$ Mpc in spite of our fitting range, which also supports our galaxy model. Figure 8 shows the 2D correlation function for the best models. We can see an excellent correspondence between the observation and our $\alpha = 1.5$ model at small scales. We see some deviation beyond $10\,h^{-1}$ Mpc, but this will be within the 1σ uncertainty, as explained in Figure 7.

5. Discussions

5.1. Interpretation of b_v^s and Ω_m

As we have seen in the previous section, the inferred velocity bias is $b_v^s = 0.982 \pm 0.040$ for $\alpha = 1.5$. This value is slightly smaller than 1, but the deviation is not significant for the size of the statistical error. We will discuss how this result compares with other studies. As we mentioned in Section 2.4, our parameter b_v^s is different from the definition used in the literature. The velocity bias is usually defined as the velocity of the visible part of the galaxies relative to the DM velocity dispersion inside their halos. Thus, it is the multiplication of two factors: the velocity bias of the baryonic component of galaxies (i.e., the observed galaxies) with respect to the whole galaxies (represented by MBPs) and the MBPs' velocity bias relative to the DM velocity dispersion. The sources of the galaxy velocity bias are also separated into two classes. The first one is related to gravitational interactions such as dynamical friction, tidal stripping, and mergers. The other includes baryonic effects such as star formation, radiative cooling, feedback from stars/supernovae/active galactic nuclei (AGNs), and heat dissipation. Given the fact that N-body simulations implement all gravitational effects, the velocity of MBPs should reflect the velocity bias induced by gravitational

interactions. Since we have defined b_v^s as the ratio between the velocity of the baryonic component of galaxies and MBPs, b_v^s will indicate the velocity bias generated by hydrodynamic effects. Figure 1 shows that the median velocity of MBPs for satellite galaxies is 0.94 of the DM velocity dispersion. As a result, the total velocity bias amounts to $0.94 \times 0.982 = 0.93$ and is broadly consistent with the one obtained by Guo et al. (2015). Our results imply that the satellite velocity bias is attributed more to dynamical effects than baryonic effects.

Munari et al. (2013) ran *N*-body simulations with and without baryon cooling, star formation, and supernova and AGN feedback. Although it is not straightforward to compare their results with ours due to the different host halo mass focused on, their Figure 8 suggests an ∼10% reduction of the velocity bias for the simulation with hydrodynamic effects. This is because the star formation and radiative emission cool galaxies down, forming a dense core and making galaxies resistant to tidal stripping. Tidal stripping selectively disrupts slow-moving galaxies, leading to higher mean galaxy velocity. Thus, adding baryon cooling counteracts it and thereby reduces the average velocity. Wu et al. (2013) investigated the effect of baryons on the galaxy velocity in their simulations, finding that the reduction of galaxy velocity depends on the distance from the cluster center, from 30% (close to halo center) to 0% (at the virial radius of host halos). They suggested that the reasoning for their result is similar to that of Munari et al. (2013) but also mentioned the baryon dragging (Puchwein et al. 2005). Considering that the fraction of satellite galaxies enclosed within the innermost region around the halo center is subdominant (Watson et al. 2012), the average reduction would be at most 10%. Ye et al. (2017) found that the velocity bias depended on the ratio between the stellar mass and host halo mass, implying that the velocity bias is mostly caused by dynamical effects. They argued that the dependence on stellar mass is a result of dynamical friction (a high-mass galaxy suffers from losing energy due to the two-body problem), and the dependence on host halo mass is related to the halo formation time (a high-mass halo is formed late, giving less time for dynamical effects to operate). All of these studies indicate that the velocity reduction caused by baryonic physics will be less significant than that caused by dynamical effects, which agrees with our results. Ye et al. (2017) also found that the velocity bias was a complicated function of other physical quantities, including age and color. Future studies can include investigating such a dependence because knowing the detailed properties of the galaxy velocity bias would be useful for future surveys such as DESI and PFS, most of which apply color selections of galaxies to define the observation strategies. It would also push forward our understanding of the kinematic perspectives of the galaxy formation and evolution. For instance, we can classify galaxies by age using the spectral energy distribution fitting technique and measure the velocity bias through clustering measurements for each class.

Our constraint on Ω_m is 0.272 ± 0.013 when we use $\alpha = 1.5$. The value is consistent with the WMAP5 result ($\Omega_m = 0.26$; Dunkley et al. 2009) but lower than that of the Planck ($\Omega_m = 0.31$; Planck Collaboration et al. 2018). In our simulation, the normalization of the power spectrum is set to give $\sigma_8 = 0.79$, which is lower than the Planck results. Thus, the correlation functions of our simulations are systematically weaker. As we saw in Figures 3 and 4, the correlation is stronger for lower Ω_m, which explains our Ω_m consistent with the WMAP5 rather than the Planck. While we only run five simulations due to the large amount of resources required, efficient methods of searching parameter space using *N*-body simulations are being studied by several projects (Nishimichi et al. 2019; DeRose et al. 2019). A more comprehensive study, including other cosmological parameters, would be beneficial.

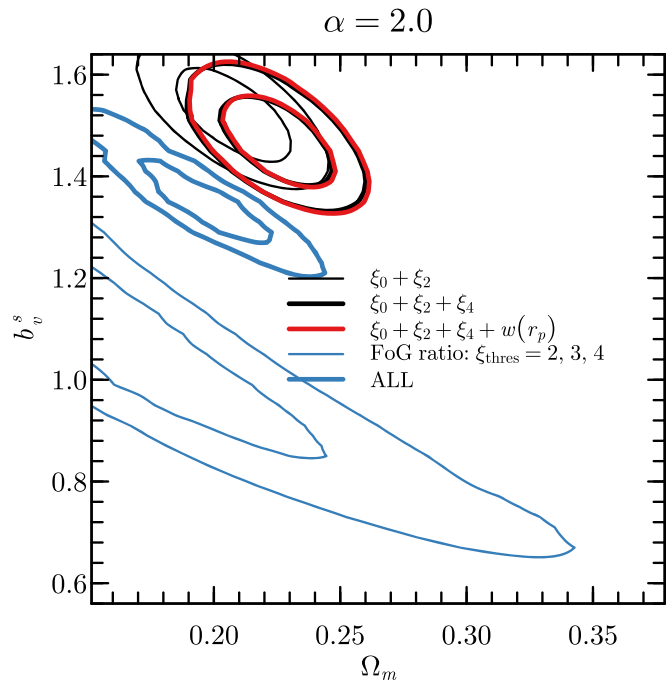

Figure 9. Same as Figure 6 but for the case of $\alpha = 2.0$. Note that the contour from the FoG ratio disagrees with those from others.

5.2. The Usefulness of the FoG Ratio

We have introduced a measure of the FoG strength as Equation (8). As discussed in Park (2000) and Tinker (2007), taking a ratio removes the dependence on the overall amplitude of the real-space correlation function. The clustering amplitude depends on cosmological parameters such as Ω_m, σ_8, and the linear growth rate f, which we usually wish to constrain, but also on unwanted factors including cosmic variance and some sort of systematic error. The cosmological parameters inferred from only the multipole moments and projected 2pCF can be contaminated by the latter factors. On the other hand, the FoG ratio is free from these uncertainties after division if these factors are universal. As seen in the previous section, we should note that the constraining power is not strong because our FoG ratio uses the correlation function along the $\mu = 0$ and 1 directions only.

The FoG ratio depends on cosmological parameters differently from the multipoles and projected 2pCF. Figure 9 shows the probability distribution of (Ω_m, b_v^s) for $\alpha = 2.0$, which is to be compared with Figure 6. In each figure, combining ξ_l and $w(r_p)$ gives preferred values of (Ω_m, b_v^s). However, the contour from the FoG ratio disagrees with those from the others in the $\alpha = 2$ case, which supports $\alpha = 1.5$. Noticeably, the contours from correlation functions and the FoG ratio shift toward different directions when the parameters are changed.

For the case of $\xi_l + w(r_p)$, increasing α results in lower Ω_m but higher b_v^s. The reason is as follows. There are more satellite galaxies when α is increased, leading to a higher amplitude of the correlation function. On the other hand, increasing Ω_m decreases the amplitude of the galaxy 2pCF (see Figure 3). This is because we fix σ_8, which means that the integration of the correlation over all scales remains the same. Increasing Ω_m increases the amplitude on very large scales, thus decreasing the correlation at the scales of our interest. Therefore, α and Ω_m are anticorrelated. In contrast, the positive correlation between α and b_v^s stems from the amplitudes of ξ_l. Considering the error bars of the observation, our constraints mainly come from $\sim$1–3 h^{-1} Mpc. At such scales, increasing b_v^s reduces ξ_l due to the enhanced FoG effect, which compensates for the α increment. The degeneracies between the three parameters are the result of the fact that ξ_l and $w(r_p)$ depend on the overall clustering amplitude, unlike the FoG ratio. Increasing both α and b_v^s indeed results in a too-strong FoG effect, which can be seen in Figure 8.

For the FoG ratio, on the other hand, an increase in α decreases both Ω_m and b_v^s. This behavior is easily understood. Increasing α increases the number of satellite galaxies, resulting in stronger FoG. In order to cancel this out, both Ω_m and b_v^s need to be smaller. Since the FoG ratio does not depend on the overall clustering amplitude, how the parameters degenerate with one another is totally different from the 2pCFs. Although we have mainly used $\alpha = 1.5$ in our study, the FoG ratio will tighten the constraints if we allow α to vary. Changing α alters the galaxy–halo connection, which is equivalent to changing the HOD parameters in that framework. Therefore, the FoG ratio would also help to constrain the parameters in the HOD approach. Another benefit of adding the FoG ratio would be that it gives a consistency check. In the absence of the cosmic variance and systematic errors, $w(r_p)$, ξ_l, and the FoG ratio overlap in the parameter space if the correct model is chosen. However, since $w(r_p)$ and ξ_l are subject to the uncertainties of the clustering amplitude while the FoG ratio is not, a discrepancy would be seen in the presence of systematic errors caused by the cosmic variance, observations, and data processing and analysis, even if the employed fitting model were sufficiently accurate.

6. Conclusions

The small-scale galaxy clustering can provide a wealth of information about the cosmological model and galaxy–halo connection owing to the availability of precise measurements. In this study, we used the Multiverse Simulation (Shin et al. 2017; Park et al. 2019), the HR4 Simulation (Kim et al. 2015), and a physically motivated galaxy assignment scheme (Hong et al. 2016) to study the small-scale redshift-space clustering. Specifically, we measured the projected correlation function $w(r_p)$ and the multipole moments $\xi_l(s)$ of the correlation function from 1.4 to 30 h^{-1} Mpc to examine their dependence on the matter density parameter Ω_m and the merger timescale parameter α. We also implemented the satellite velocity bias parameter b_v^s to account for the possible velocity difference between galaxies and DM inside halos (Munari et al. 2013; Wu et al. 2013; Guo et al. 2015; Ye et al. 2017). We have measured the correlation functions of a volume-limited sample from the KIAS-VAGC catalog (Choi et al. 2010), which is based on the SDSS DR7 spectroscopic data, to compare with those of the Multiverse Simulation. In the comparison, we have newly defined the strength of the FoG effect, $R_{|\xi}$, which is free from the change in the overall amplitude of the correlation function due to the cosmic variance and systematic errors. We have found that $\alpha = 1.5$ reproduces the observation well, with $(\Omega_m, b_v^s) = (0.272 \pm 0.013, 0.982 \pm 0.040)$. While our b_v^s broadly agreed with previous observational and simulation studies (Munari et al. 2013; Wu et al. 2013; Guo et al. 2015; Ye et al. 2017), Ω_m was smaller than the Planck results (Planck Collaboration et al. 2018), which we attributed to the lower σ_8 that we assumed in the Multiverse Simulations. Considering that the velocities of MBPs for satellite galaxies are 0.93 of that of DM, the slow motions of galaxies relative to the DM velocity dispersion found by Guo et al. (2015) are mainly caused by dynamical effects rather than baryonic effects. The FoG ratio was found to be useful to break the degeneracy between the parameters and can be used to check the consistency of the fit obtained by $w(r_p)$ and $\xi_l(s)$.

We thank Christophe Pichon for fruitful discussions of this work and Junsup Shim for useful comments on the paper. H.P. acknowledges support by the World Premier International Research Center Initiative (WPI), MEXT, Japan. S.E.H. was supported by the Basic Science Research Program through the National Research Foundation of Korea funded by the Ministry of Education (2018R1A6A1A06024977).

The authors acknowledge the Korea Institute for Advanced Study for providing computing resources (KIAS Center for Advanced Computation Linux Cluster System). This work was supported by the Supercomputing Center/Korea Institute of Science and Technology Information, and supercomputing resources including technical support (KSC-2016-C3-0071) and the simulation data were transferred through a high-speed network provided by KREONET/GLORIAD.

Funding for the SDSS and SDSS-II has been provided by the Alfred P. Sloan Foundation, the Participating Institutions, the National Science Foundation, the US Department of Energy, the National Aeronautics and Space Administration, the Japanese Monbukagakusho, the Max Planck Society, and the Higher Education Funding Council for England. The SDSS website is http://www.sdss.org/.

The SDSS is managed by the Astrophysical Research Consortium for the Participating Institutions. The Participating Institutions are the American Museum of Natural History, the Astrophysical Institute Potsdam, the University of Basel, the University of Cambridge, Case Western Reserve University, the University of Chicago, Drexel University, Fermilab, the Institute for Advanced Study, the Japan Participation Group, Johns Hopkins University, the Joint Institute for Nuclear Astrophysics, the Kavli Institute for Particle Astrophysics and Cosmology, the Korean Scientist Group, the Chinese Academy of Sciences (LAMOST), Los Alamos National Laboratory, the Max Planck Institute for Astronomy (MPIA), the Max Planck Institute for Astrophysics (MPA), New Mexico State University, Ohio State University, the University of Pittsburgh, the University of Portsmouth, Princeton University, the US Naval Observatory, and the University of Washington.

Appendix A
The χ^2 Statistics

Table A1 shows the minimum χ^2 values and those per degree of freedom (dof), obtained from Equation (9) for different sets of measurements. The best-fit χ^2/dof is 1.67 for

Table A1
The χ^2 Values (Top) and χ^2 per dof (Bottom) for the Best-fit (Ω_m, b_v^s) Cases for $\alpha = 1.5$ and 2.0

	$\alpha = 1.5$	$\alpha = 2.0$
w	5.50	6.73
$\xi_0 + \xi_2$	13.08	25.27
$\xi_0 + \xi_2 + \xi_4$	43.03	108.55
$\xi_0 + \xi_2 + \xi_4 + w$	47.45	114.56
$\xi_0 + \xi_2 + \xi_4 + w$ + FoG	55.03	171.02
w	0.92	1.12
$\xi_0 + \xi_2$	0.93	1.81
$\xi_0 + \xi_2 + \xi_4$	1.96	4.93
$\xi_0 + \xi_2 + \xi_4 + w$	1.58	3.82
$\xi_0 + \xi_2 + \xi_4 + w$ + FoG	1.67	5.18

the case where we use all measurements, which might be slightly high. Here we give some possible reasons by discussing our statistical treatment and suggest several ways to improve it.

First, we used the covariance matrix estimated from the mock galaxy catalogs rather than jackknife resampling. We have also measured the covariance matrix using the jackknife method and found that the diagonal elements from the mocks are about half of those from the jackknife method, which means that the size of our error bars is smaller by a factor of $\sqrt{2}$. Because doubling the covariance matrix halves χ^2, this partly describes the different χ^2 values obtained by Guo et al. (2015) and us. Then, why are the values of the covariance matrix from mock catalogs smaller than the jackknife resampling? One reason is related to the inherent feature of the jackknife; Norberg et al. (2009) demonstrated that the jackknife returned the error bars accurately beyond $\sim 10\,h^{-1}$ Mpc but significantly overestimated those below $10^{0.5}\,h^{-1}$ Mpc for both $w(r_p)$ and $\xi(s)$, where our constraints mainly come from. Another possible reason is specific to our data; it includes the Sloan Great Wall (Gott et al. 2005), which is centered at $z = 0.08$. The unusually huge structure may lead to the large region-to-region variance, enhancing the error bars from the jackknife.

Sinha et al. (2018) investigated the effect of the noise from the limited number of mocks on the resulting χ^2. Due to the nonlinearity of the inverse operation of the covariance matrix, this kind of noise enters into a χ^2 analysis in an unpredictable manner. Sinha et al. (2018) provided a solution to use principal component analysis to extract some eigenvectors with large signal-to-noise ratios and obtained smaller χ^2/dof values.

As is obvious from Table A1, ξ_4 contributes hugely to the large χ^2 that we obtain. However, Figure 6 shows that the inclusion of ξ_4 does not improve the constraining power. These facts might mean that the information of ξ_4 is already included in the combination of ξ_0 and ξ_2, or our model is insufficient to reproduce up to ξ_4. Improvements of our model can include allowing the central galaxy velocity bias parameter b_v^c to change, but we will only try $b_v^c = 0$ in the next appendix and leave the detailed analysis to future works.

Appendix B
The Model with Zero Central Galaxy Velocity Bias

While we have assumed $\boldsymbol{v}^g \sim \boldsymbol{v}^{\mathrm{MBP}}$ for central galaxies in the main text, we show the fitting result when the central velocity bias $b_v^c = 0$; i.e., the central galaxies are rest at the center of halos (b_v^c is defined similarly to Equation (4)). Figure B1 shows the χ^2 contour obtained in the same manner as Figure 6. Although the final constraint (bold blue line) is apparently consistent with that in the main text, it is simply a coincidence because the contours for ξ_l do not overlap one another.

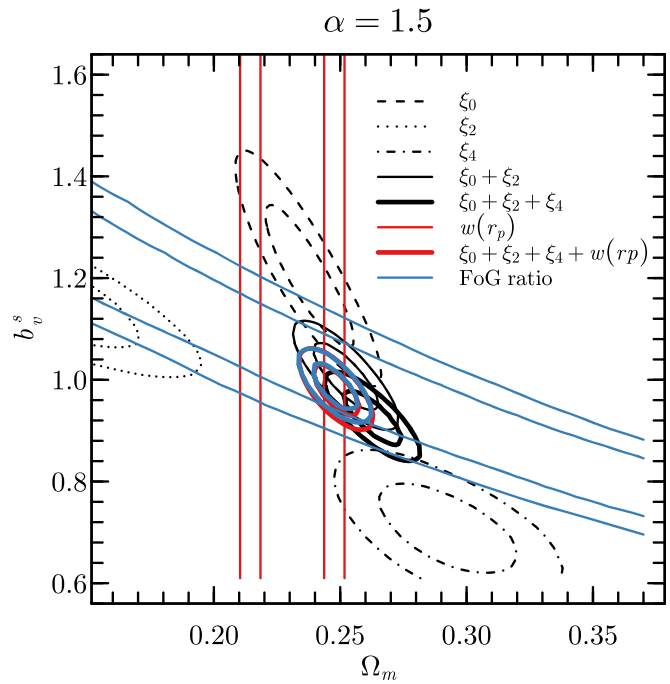

Figure B1. Similar to Figure 6, but $b_v^c = 0$ is assumed. Note that only the diagonal elements of the covariance matrix are used.

The shift of the FoG ratio (thin blue line) can be interpreted easily, owing to the fact that the FoG ratio is a pure measurement of FoG. The degree of the FoG effect is governed by the quadratic sum of the velocities of central and satellite galaxies. Therefore, b_v^s has to be larger to compensate for nullifying central galaxy velocities inside halos. On the other hand, understanding the shifts of the correlation functions is not straightforward. On small scales, the higher velocity bias takes the galaxy pairs to large separations in redshift space, reducing the amplitudes of ξ_l. Similar to the FoG ratio, the decrease of the central galaxy velocity can be partly canceled out by the increase of the satellite velocity bias. However, not only the increase of b_v^s but also the decrease in Ω_m can increase the correlation amplitudes at such scales. Furthermore, the data points from larger scales have to be fit simultaneously, making the degeneracy of (Ω_m, b_v^c, b_v^s) complicated when we use the correlation functions.

Note that only the diagonal elements of the covariance matrix are used to produce Figure B1. Due to the strong correlation and anticorrelation between each bin of ξ_l and $w(r_p)$, the off-diagonal elements of $\mathbb{C}^{-1}$ are noisy. If the theoretical model were reasonably correct, the contributions of off-diagonal elements to $[\boldsymbol{X}^{\mathrm{obs}} - \boldsymbol{X}^{\mathrm{th}}(\boldsymbol{\theta})]^T \mathbb{C}^{-1} [\boldsymbol{X}^{\mathrm{obs}} - \boldsymbol{X}^{\mathrm{th}}(\boldsymbol{\theta})]$ would not affect the best-fit values significantly because $|\boldsymbol{X}^{\mathrm{obs}} - \boldsymbol{X}^{\mathrm{th}}(\boldsymbol{\theta})|$ is small. While we have confirmed that the best-fit values in the main text were stable even if we used only the diagonal components, we found that the bold blue line was far from the rest of the contours when we used the full

covariance matrix here. This implies that $a_c = 0$ is not a good model, probably giving unstable behaviors of the off-diagonal component of $[\boldsymbol{X}^{\rm obs} - \boldsymbol{X}^{\rm th}(\boldsymbol{\theta})]^T \mathbb{C}^{-1}[\boldsymbol{X}^{\rm obs} - \boldsymbol{X}^{\rm th}(\boldsymbol{\theta})]$ caused by large $|\boldsymbol{X}^{\rm obs} - \boldsymbol{X}^{\rm th}(\boldsymbol{\theta})|$, which supports previous studies that claim the existence of the central galaxy velocity bias.

Appendix C
The Fiber Collision Effect

Due to the mechanical limitation of the SDSS spectroscopic instrument, when a galaxy pair is separated by an angular separation less than 55″, only either one can be observed by a single run. This is called a fiber collision effect and leads to systematics in the correlation function measurements (Zehavi et al. 2002; Guo et al. 2012). Because the so-called NN method is adopted in our study and can cause systematic errors on small-scale measurements (Reid et al. 2014), we have tested the validity of it by simulating the fiber collision effect using the HR4 simulation data. We use the concept of Guo et al. (2012) to model the fiber collision effect. The angular friends-of-friends grouping is performed for the objects on the celestial plane with a linking length of 55″. Then, the objects are classified into three groups:

1. D1: galaxies that are isolated.
2. D2: galaxies that collide with one close galaxy (typically doublets).
3. D2': galaxies that collide with more than one galaxy (typically the middle one of triplets).

We divide the HR4 galaxy catalog into 18 boxes to create "flux-limited" samples that correspond to the parent photometric catalog of the KIAS-VAGC. Specifically, we select the heaviest galaxies within the distance range, which goes from 10 to 800 Mpc h^{-1} with a bin size of 10 Mpc h^{-1} to obtain the same number density. Because the fiber collision occurs in the parent photometric catalog before any redshift and luminosity cut, we require much more distant galaxies, which leads to the small number of realizations (18) compared to the ones for the covariance matrix (405).

We apply this classification to the KIAS-VAGC parent catalog to estimate the fraction of fiber-allocated galaxies as a function of the population (D1, D2, or D2') and the number of plates covering the position of objects ($N_{\rm tile}$). Then, for each of the 18 realizations, the same classification code is run, and "observed" galaxies are determined according to these fractions.

Then, we assign the NN redshift to the "unobserved" galaxies, apply the redshift and mass cut, and measure the correlation functions. The comparison is given in Figures C1 and C2. We also perform another fiber collision correction method based on the pairwise inverse probability (PIP) weights (Bianchi & Percival 2017). In this case, we repeat the selection process 1000 times to create the logical array of length $N_{\rm bits} = 1000$ for each galaxy, each element of which is either zero (unobserved) or 1 (observed). The correlation function is then measured using the pairwise weight given by Equation (14) of Bianchi & Percival (2017).

The PIP scheme is accurate over almost all scales, as it is an unbiased way of correcting for the missing observations. The NN method is, however, still possible to use for our interested scales. This result is different from the argument of Reid et al. (2014) but can be explained by the difference of the minimum scale probed and the different collision scale in the comoving space (<0.1 and <0.4 Mpc h^{-1} for our and their works, respectively). While the higher-redshift data such as BOSS and eBOSS would require the PIP method for small-scale clustering study, the NN method suffices for our study.

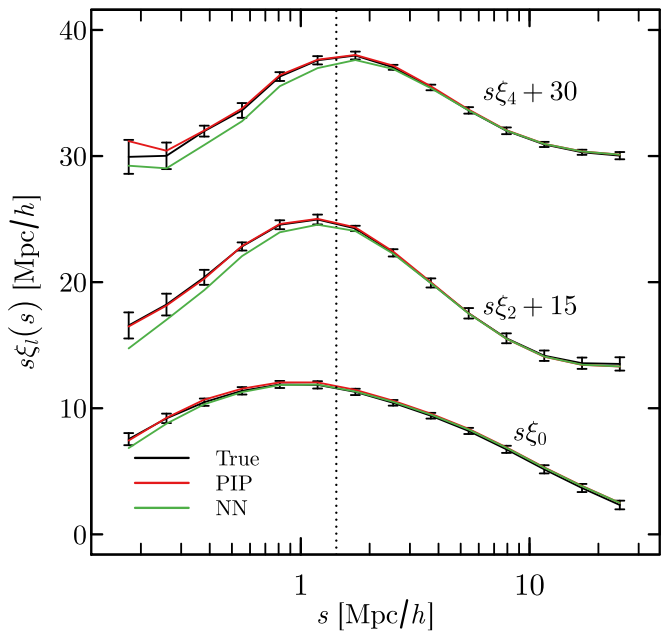

Figure C1. Fiber collision effect on the multipole moments. The black lines are the fiducial data from the HR4 galaxy sample that we want to recover, while the red and green lines are obtained by simulating the PIP and NN schemes for the fiber collision correction, respectively. The vertical line shows the minimum scale for our analysis in the main text. We adopt the NN scheme in this study.

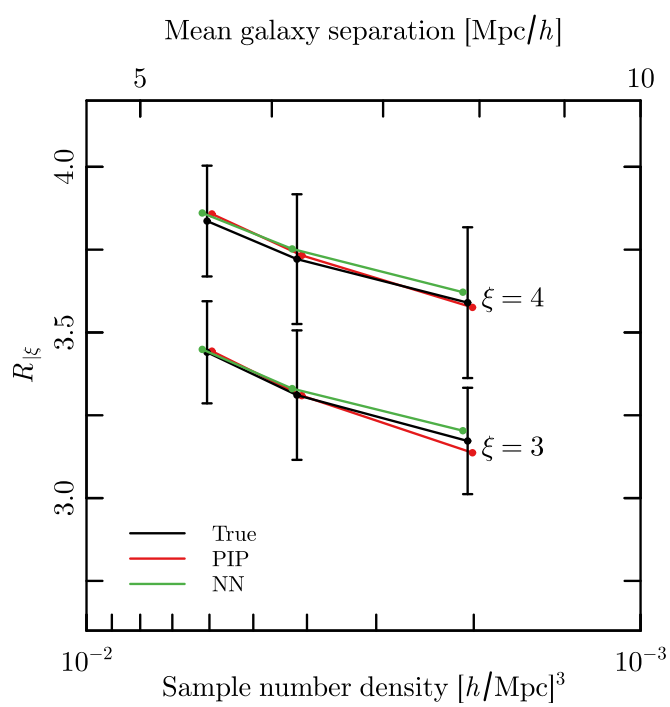

Figure C2. Fiber collision effect on the FoG ratio. We show two threshold levels, $\xi = 3$ and 4. The x-axis gives the sample number density. For our sample in the text, it is 6.1×10^{-3} (h^{-1} Mpc)^3 and corresponds to the leftmost points. The black lines are the fiducial data from the HR4 galaxy sample that we want to recover, while the red and green lines are obtained by simulating the PIP and NN schemes for the fiber collision correction, respectively. We adopt the NN scheme in this study.

ORCID iDs

Changbom Park https://orcid.org/0000-0001-9521-6397
Hyunbae Park (박현배) https://orcid.org/0000-0002-7464-7857
Sungwook E. Hong (홍성욱) https://orcid.org/0000-0003-4923-8485
Ho Seong Hwang https://orcid.org/0000-0003-3428-7612
Juhan Kim (김주한) https://orcid.org/0000-0002-4391-2275

References

Abazajian, K. N., Adelman-McCarthy, J. K., Agüeros, M. A., et al. 2009, ApJS, 182, 543
Alam, S., Zhu, H., Croft, R. A. C., et al. 2017, MNRAS, 470, 2822
Appleby, S., Chingangbam, P., Park, C., et al. 2018, ApJ, 863, 200
Beltz-Mohrmann, G. D., Berlind, A. A., & Szewciw, A. O. 2020, MNRAS, 491, 5771
Beutler, F., Blake, C., Colless, M., et al. 2012, MNRAS, 423, 3430
Beutler, F., Saito, S., Seo, H.-J., et al. 2014, MNRAS, 443, 1065
Bianchi, D., & Percival, W. J. 2017, MNRAS, 472, 1106
Bianchi, D., Percival, W. J., & Bel, J. 2016, MNRAS, 463, 3783
Blake, C., Brough, S., Colless, M., et al. 2011, MNRAS, 415, 2876
Blanton, M. R., Schlegel, D. J., Strauss, M. A., et al. 2005, AJ, 129, 2562
Choi, Y.-Y., Han, D.-H., & Kim, S. S. 2010, JKAS, 43, 191
Davis, M., Efstathiou, G., Frenk, C. S., & White, S. D. M. 1985, ApJ, 292, 371
Dawson, K. S., Kneib, J.-P., Percival, W. J., et al. 2016, AJ, 151, 44
Dawson, K. S., Schlegel, D. J., Ahn, C. P., et al. 2013, AJ, 145, 10
DESI Collaboration, Aghamousa, A., Aguilar, J., et al. 2016, arXiv:1611.00036
de la Torre, S., Guzzo, L., Peacock, J. A., et al. 2013, A&A, 557, A54
DeRose, J., Wechsler, R. H., Tinker, J. L., et al. 2019, ApJ, 875, 69
Drinkwater, M. J., Jurek, R. J., Blake, C., et al. 2010, MNRAS, 401, 1429
Dunkley, J., Komatsu, E., Nolta, M. R., et al. 2009, ApJS, 180, 306
Feldman, H., Juszkiewicz, R., Ferreira, P., et al. 2003, ApJL, 596, L131
Frieman, J. A., Turner, M. S., & Huterer, D. 2008, ARA&A, 46, 385
Geller, M. J., Diaferio, A., & Kurtz, M. J. 2011, AJ, 142, 133
Gott, J. R., III, Jurić, M., Schlegel, D., et al. 2005, ApJ, 624, 463
Guo, H., Zehavi, I., & Zheng, Z. 2012, ApJ, 756, 127
Guo, H., Zheng, Z., Zehavi, I., et al. 2015, MNRAS, 453, 4368
Guzzo, L., Pierleoni, M., Meneux, B., et al. 2008, Natur, 451, 541
Guzzo, L., Scodeggio, M., Garilli, B., et al. 2014, A&A, 566, A108
Hamilton, A. J. S. 1998, The Evolving Universe, Vol. 231 (Dordrecht: Kluwer), 185
Hartlap, J., Simon, P., & Schneider, P. 2007, A&A, 464, 399
Hawkins, E., Maddox, S., Cole, S., et al. 2003, MNRAS, 346, 78
Hong, S., Jeong, D., Hwang, H. S., et al. 2020, MNRAS, 493, 5972
Hong, S. E., Park, C., & Kim, J. 2016, ApJ, 823, 103
Hwang, H. S., Geller, M. J., Park, C., et al. 2016, ApJ, 818, 173
Icaza-Lizaola, M., Vargas-Magaña, M., Fromenteau, S., et al. 2020, MNRAS, 492, 4189
Jackson, J. C. 1972, MNRAS, 156, 1
Jiang, C. Y., Jing, Y. P., Faltenbacher, A., Lin, W. P., & Li, C. 2008, ApJ, 675, 1095
Jones, D. H., Saunders, W., Read, M., & Colless, M. 2005, PASA, 22, 277
Joyce, A., Lombriser, L., & Schmidt, F. 2016, ARNPS, 66, 95
Juszkiewicz, R., Fisher, K. B., & Szapudi, I. 1998, ApJL, 504, L1
Kaiser, N. 1987, MNRAS, 227, 1
Kim, J., Park, C., Gott, J. R., III, & Dubinski, J. 2009, ApJ, 701, 1547
Kim, J., Park, C., L'Huillier, B., & Hong, S. E. 2015, JKAS, 48, 213
Koyama, K. 2016, RPPh, 79, 046902
Kuruvilla, J., & Porciani, C. 2018, MNRAS, 479, 2256
Landy, S. D., & Szalay, A. S. 1993, ApJ, 412, 64
Li, X.-D., Park, C., Sabiu, C. G., et al. 2016, ApJ, 832, 103
Linder, E. V. 2005, PhRvD, 72, 043529
Marzke, R. O., Geller, M. J., da Costa, L. N., & Huchra, J. P. 1995, AJ, 110, 477
Montero-Dorta, A. D., Perez, E., Prada, F., et al. 2017, ApJL, 848, 2
Munari, E., Biviano, A., Borgani, S., Murante, G., & Fabjan, D. 2013, MNRAS, 430, 2638
Ng, P. T., & Maechler, M. 2020, COBS – Constrained B-splines (Sparse matrix based). R package, v.1.3-4
Nishimichi, T., Takada, M., Takahashi, R., et al. 2019, ApJ, 884, 29
Norberg, P., Baugh, C. M., Gaztañaga, E., & Croton, D. J. 2009, MNRAS, 396, 19
Okumura, T., Hikage, C., Totani, T., et al. 2016, PASJ, 68, 38
Park, C. 2000, MNRAS, 319, 573
Park, C., & Choi, Y.-Y. 2009, ApJ, 691, 1828
Park, C., & Kim, Y.-R. 2010, ApJL, 715, L185
Park, H., Park, C., Sabiu, C. G., et al. 2019, ApJ, 881, 146
Perlmutter, S., Aldering, G., Goldhaber, G., et al. 1999, ApJ, 517, 565
Planck Collaboration, Aghanim, N., Akrami, Y., et al. 2018, arXiv:1807.06209
Puchwein, E., Bartelmann, M., Dolag, K., & Meneghetti, M. 2005, A&A, 442, 405
Reid, B. A., Samushia, L., White, M., et al. 2012, MNRAS, 426, 2719
Reid, B. A., Seo, H.-J., Leauthaud, A., et al. 2014, MNRAS, 444, 476
Riess, A. G., Filippenko, A. V., Challis, P., et al. 1998, AJ, 116, 1009
Samushia, L., Percival, W. J., & Raccanelli, A. 2013, MNRAS, 420, 2102
Sánchez, A. G., Scoccimarro, R., Crocce, M., et al. 2017, MNRAS, 464, 1640
Sargent, W. L. W., & Turner, E. L. 1977, ApJL, 212, 3
Sheth, R. K. 1996, MNRAS, 279, 1310
Shin, J., Kim, J., Pichon, C., et al. 2017, ApJ, 843, 73
Sinha, M., Berlind, A. A., McBride, C. K., et al. 2018, MNRAS, 478, 1042
Spergel, D., Gehrels, N., Baltay, C., et al. 2015, arXiv:1503.03757
Takada, M., Ellis, R. S., Chiba, M., et al. 2014, PASJ, 66, R1
Taruya, A., Nishimichi, T., & Saito, S. 2010, PhRvD, 82, 063522
Tinker, J. L. 2007, MNRAS, 374, 477
Tonegawa, M., Totani, T., Okada, H., et al. 2015, PASJ, 67, 81
Vikhlinin, A., Kravtsov, A. V., Burenin, R. A., et al. 2009, ApJ, 692, 1060
Wang, L., Weinmann, S. M., de Lucia, G., & Yang, X. 2013, MNRAS, 433, 515
Watson, D. F., Berlind, A. A., McBride, C. K., et al. 2012, ApJ, 749, 83
Weinberg, D. H., Mortonson, M. J., Eisenstein, D. J., et al. 2013, PhR, 530, 87
Wu, H.-Y., Hahn, O., Evrard, A. E., Wechsler, R. H., & Dolag, K. 2013, MNRAS, 436, 460
Ye, J.-N., Guo, H., Zheng, Z., & Zehavi, I. 2017, ApJ, 841, 45
York, D. G., Adelman, J., Anderson, J. E., Jr., et al. 2000, AJ, 120, 1579
Zehavi, I., Blanton, M. R., Frieman, J. A., et al. 2002, ApJ, 571, 172
Zheng, Z., & Guo, H. 2016, MNRAS, 458, 4015